Received July 22, 2020, accepted August 28, 2020, date of publication September 3, 2020, date of current version September 22, 2020.

Digital Object Identifier 10.1109/ACCESS.2020.3021418

Advanced Processing of 3D Computational Microwave Polarimetry Using a Near-Field Frequency-Diverse Antenna

RIXI PENG[1], OKAN YURDUSEVEN[2], (Senior Member, IEEE), THOMAS FROMENTEZE[3], AND DAVID R. SMITH[1], (Senior Member, IEEE)

[1]Center for Metamaterial and Integrated Plasmonics, Department of Electrical and Computer Engineering, Duke University, Durham, NC 27708, USA
[2]Centre for Wireless Innovation, School of Electronics, Electrical Engineering and Computer Science, Institute of Electronics, Communications and Information Technology, Queens University Belfast, Belfast BT3 9DT, U.K.
[3]University of Limoges, XLIM, UMR 7252, F-87000 Limoges, France

Corresponding author: Rixi Peng (rixi.peng@duke.edu)

This work was supported in part by the U.S. Air Force Office of Scientific Research (AFOSR) under Grant FA9550-12-1-0491.

ABSTRACT Polarimetry is typically restricted to far-field characterization of a target using beam-like waves, which results in a 2×2 scattering matrix representation under two orthogonal in-plane polarization bases. However, a short-range (or radiative near-field) microwave polarimetric approach can recover a 3×3 polarimetric matrix representing a full vector polarimetric response of the imaged object. The computational imaging method retrieves this full polarimetric response by utilizing an ensemble of randomly polarized probing fields from a cavity-backed metasurface antenna as the enabling technology. In this paper, we describe the polarization states of the non-planar vector sensing fields with three-dimensional (3D) Jones vectors and examine the polarization diversity with the polarization ellipses in 3D space. Corresponding 3D polarimetric target parameters are derived from the 3D polarimetric matrix and the diagonalization process of this matrix. The generalized 3D target parameters disclose direct details of the imaged object which are otherwise inaccessible to the conventional 2×2 polarimetric scattering matrix description, especially the polarimetric features along the range direction. The target parameters reconstructed in experiments validate the effectiveness of our 3D polarimetric near-field imaging framework and the parameterization. The advanced processing and parameterization of 3D polarimetry indicate great potential applications in many short-range microwave imaging scenarios.

INDEX TERMS Microwave polarimetry, computational imaging, radiative near field, electromagnetic metasurface.

I. INTRODUCTION

Polarimetric microwave imaging exploits the vector nature of electromagnetic waves to measure scattering responses of a target using different polarization combinations of the transmitter and the receiver. Many aspects, including geometrical and electrical characteristics of scatterers and the observation geometry, can contribute to the complicated local scattering response of the target [1], [2]. With interpretation of the polarimetric response by separating these aspects, polarimetric imaging has shown to unveil more characteristics of the target-wave interaction than purely scalar microwave imaging [3], [4]. In conventional microwave polarimetry, the polarimetric signature of the target can be represented by a 2×2 scattering matrix, which is commonly measured by four combinations of two orthogonal polarization states of the transmitting and receiving antennas. For more general scenario, a covariance matrix or a Mueller matrix is used to describe the spatially averaged polarimetric responses of distributed targets in multi-looked imaging [5], [6]. Due to the complexity of local polarimetric scattering mechanism, it is challenging to interpret the complex scattering matrix or other formats of scattering matrices intuitively. Polarimetric target decomposition methods, first formalized by Huynen [7], aim at extracting physical target parameters from the polarimetric scattering matrices [8]. Common polarimetric target decomposition methods include model-based decomposition, such as Freeman-Durden three-component

The associate editor coordinating the review of this manuscript and approving it for publication was Muhammad Zubair.

decomposition [9], and eigendecomposition analysis, such as Cloude decomposition [10]. With the advent of these target decomposition methods, microwave polarimetry, e.g., polarimetric synthetic aperture radar (PolSAR), has demonstrated a plethora of applications in remote sensing, agriculture and geoscience, including terrain and land-use classification [11]–[13], soil moisture assessment [14], [15], and ocean surface observation [16], [17]. Despite plenty of applications, polarimetry imaging is restricted to characterizing the scene with only the cross-range components in the far-field of the antenna. This limitation drives the research interest of implementing three-dimensional(3D) full vector polarimetry imaging, where a nontrivial target response along with the range direction, can be retrieved. This 3D polarimetry requires new description for the polarization states of waves and the corresponding polarimetric scattering response of the target other than the established methodology for conventional far-field polarimetry. In the optical range, some theoretical analyses and experimental demonstrations, e.g. in a reverberating chamber, have been made to extend the polarization description to non-planar waves [18]–[21]. Here, we use 3D Jones vector description of the sensing fields along with a 3×3 susceptibility tensor of the target for the microwave polarimetric imaging. 3D polarimetry depends on the sensing fields with all three vector components of the field. In our preliminary study [22], we exploit the non-planar nature of radiative near field of a cavity-backed antenna along with the computational imaging concept to achieve 3D polarimetric imaging with significant simplification of the hardware. Computational imaging leverages optimization algorithms for inverse problems and advancing computation resources to transform the imaging system configuration and the process of interrogating the scene [23]–[27]. This technique aims to circumvent some limitations faced by conventional imaging methods, for example, large spatial-bandwidth-product(SBP) imaging [28], [29] which achieves high resolution and wide field simultaneously, or to noticeably simplify the system hardware requirement with drastically reduced cost, e.g., single-pixel imaging [30]–[32]. Computational imaging paradigm typically encodes the signal of interest into a series of indirect measurements, often in compressive sensing fashion, and reconstructs the scene by solving an optimization problem. In our system, we use an ensemble of random sensing fields with frequency, spatial and polarization diversity to multiplex 3D polarimetric responses of an imaging domain into one single complex measurement at each frequency point over some bandwidth.

To generate the random probing field set for the 3D computational polarimetric imaging purpose, we utilize a cavity-backed metasurface aperture antenna. Metasurface antenna possesses large degrees of freedom in engineering its scattering property and has recently shown great fulfillment of demands for novel computational imaging systems [33]–[36]. Specifically, the cavity-backed metasurface aperture in our study has been demonstrated to radiate a series of pseudo-orthogonal electromagnetic field patterns indexed by the driving frequency and these patterns have sufficient spatial and frequency diversity to probe the target scene [37]. This characteristic of the metasurface aperture has further been exploited to reconstruct the reflectivity contrast and phase of the target space phase using intensity-only measurements in the microwave range [38], [39]. For the aim of polarimetric imaging, we show that the field patterns radiated by this metasurface aperture possess polarization diversity which paves the way for the compressive 3D polarimetric imaging application.

In this paper, we first revisit the architecture of computational microwave polarimetric imaging proposed in our preliminary work [22], [40]. It is demonstrated that our system has the ability to retrieve spatially-resolved three-dimensional polarimetric scattering matrices with huge simplification on the hardware. In our system, the active components necessary to reconfigure the fields interrogating the domain to be imaged are eliminated. Another simplification is that a single transmit-receive chain is used for this demonstration. It should also be noted that analogous work oriented towards the detection of non-cooperative thermal sources has allowed the reconstruction of different 2D polarization states with a cavity-backed metasurface [41]. Built on our previous work [22], [40], this paper enunciates the further physical interpretation of this 3D scattering matrix by proposing different eigendecomposition analysis compared with [22] and deriving multiple parameters which are directly related to local geometric and scattering features of the target. We characterize the 3D polarization state using the 3D Jones vector and corresponding polarization ellipses to demonstrate the underlying polarization diversity of the sensing fields. Characteristic target parameters for 3D polarimetry are developed to extract local orientation of the target in 3D space and its polarimetric scattering properties in the near-field. This target parameterization process enables the physical interpretation of the 3×3 complex scattering matrix with a series of quantitative scalar parameters in an analogy to the Huynen's decomposition in far-field polarimetry. These parameters describe the target's responses to not only different polarization states as in 2D polarimetry but also various local propagation directions of the wave. This 3D polarimetry technique and 3D target parameterization yield rich polarimetric information that can be used to enhance the contrast in the scene or obtain target features along the range direction. These pieces of information are useful in short-range imaging application scenarios, for example, concealed threat detection and classification [42]. This framework can be further translated to other application scenarios at different electromagnetic wave frequency ranges, for instance, near-field scanning optical microscopy where the electric field is in nature three-dimensional [18].

II. THREE-DIMENSIONAL POLARIZATION STATE DESCRIPTION OF RANDOM FIELDS

In this section, our computational 3D polarimetric imaging system initially introduced in [22] is first revisited for

the completion of this paper. We then elucidate the theory of the three-dimensional Jones vector and the polarization ellipse in 3D space which effectively characterizes the fully-polarized random fields. Based on these concepts, we demonstrate with 3D polarization ellipses the polarization diversity of the spatially-varying but fully-polarized random fields generated by a cavity-backed metasurface aperture antenna.

The cavity-backed metasurface aperture antenna employed is illustrated in Fig.1(a). It consists of a 28.5cm(W) $\times$ 28.5cm(L) $\times$ 15.2cm(H) high quality-factor ($Q = 12000$) air-filled metallic cavity which supports several thousands of diverse modes switched by the feeding frequency [35]. Randomized holes on the front surface of the cavity over an area of 15cm $\times$ 15cm couple out cavity modes to an ensemble of radiation patterns indexed by the feeding frequency. Two coaxial cables connect the rear surface with a vector network analyzer (VNA) which takes coherent measurements $\boldsymbol{g}(f)$ at 4001 evenly-spaced discrete frequency points f in K band ($17.5 - 26.5$GHz). This metasurface antenna radiates effectively as a collection of in-plane magnetic polarizable dipoles m_y, m_z [22]. These magnetic dipoles are characterized in the experiment by equivalently measuring the fields over the antenna aperture in its near field with an open-end waveguide antenna using a planar near-field scanner (NSI 200V). The measurements of E_y, E_z at two subsequent frequency points are shown in Fig.1(c). With a small frequency shift of 2MHz, the field patterns show a substantial difference. The three-dimensional incident fields and the receiving fields,which by reciprocity is identical to the radiated fields from the excitation of the port 2, in any domain of interest are known by computationally propagating the equivalent in-plane dipoles to the target space using dyadic Green's function [43]–[45]. With $\hat{y}, \hat{z}$ components of magnetic dipoles, the radiation fields are of three dimensions in the radiative near field. [22].

This 3D polarimetry imaging system, depicted in Fig.1, provides non-planar sensing fields radiated from the randomized cavity surface. Since the radiation field of this aperture antenna has nontrivial components of E_x, E_y, E_z due to near-field operation, we have proposed, in the preliminary study, to use the electric susceptibility tensor $\boldsymbol{\chi}$ to characterize the local scattering process in the radiative near field. Assuming first Born approximation [43], [46], the computational polarimetric imaging forward model with the full-vector random fields and the susceptibility tensor description of the target is expressed as, at each frequency f,

$$g(f) = \int_V \boldsymbol{E}_r^T(\boldsymbol{r})\boldsymbol{\chi}(\boldsymbol{r})\boldsymbol{E}_t(\boldsymbol{r})d\boldsymbol{r} \tag{1}$$

where $\boldsymbol{E}_r = [E_{x,r}, E_{y,r}, E_{z,r}]^T$ and $\boldsymbol{E}_t = [E_{x,t}, E_{y,t}, E_{z,t}]^T$ are the vector electric fields generated from exciting the receiving port or the transmitting port respectively, $\boldsymbol{\chi}$ denotes the target electric susceptibility tensor and $\boldsymbol{r}$ is the location in the scene. The susceptibility tensor $\boldsymbol{\chi}(\boldsymbol{r})$, in the Cartesian

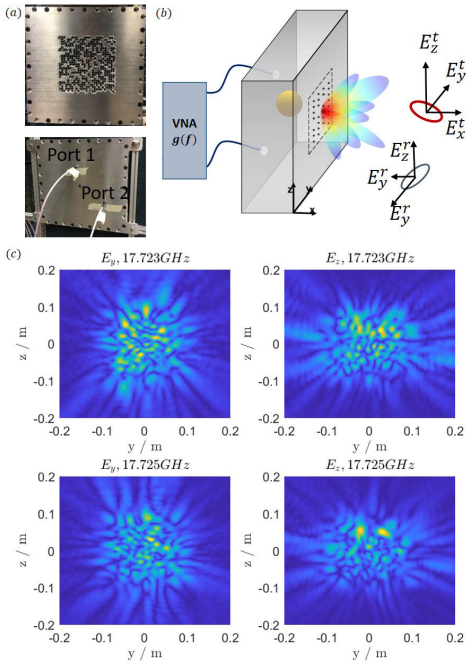

FIGURE 1. (a) Front and rear image of the cavity-backed metasurface aperture antenna.(b) Cavity-backed metasurface aperture and computational polarimetric imaging setup. Red and blue ellipses demonstrate different polarization states for the transmitting and receiving ends. (c) Near field scan results with port 1 for dual-polarization at two neighboring frequency points.

coordinates, can be expressed in the matrix format as,

$$\boldsymbol{\chi}(\boldsymbol{r}) = \begin{bmatrix} \chi_{xx} & \chi_{xy} & \chi_{xz} \\ \chi_{yx} & \chi_{yy} & \chi_{yz} \\ \chi_{zx} & \chi_{zy} & \chi_{zz} \end{bmatrix}. \tag{2}$$

If the propagation medium is reciprocal (not valid for ferro-magnetic object), the reciprocity theorem ensures the symmetry of the matrix $\boldsymbol{\chi}$, or $\chi_{xy} = \chi_{yx}, \chi_{xz} = \chi_{zx}$ and $\chi_{yz} = \chi_{zy}$. The 3D polarimetric response of the whole target scene is multiplexed by the vector field patterns $(\boldsymbol{E}_t, \boldsymbol{E}_r)$ into one single complex measurement at single frequency. With a simple frequency sweep of m points, we can obtain the compressive measurements in the format of m complex numbers $g(f_i), i = 1, 2, \ldots, m$. To recover the spatially resolved polarimetric response $\boldsymbol{\chi}(\boldsymbol{r})$ requires the knowledge of the spatially varying illumination and sensing fields $\boldsymbol{E}_r(\boldsymbol{r}), \boldsymbol{E}_t(\boldsymbol{r})$ for all the frequency points. In our system, these fields are numerically calculated by propagating the experimentally measured near fields (shown in Fig.1) to the domain of interest by using dyadic Green's function of free space. By forming a measurement vector $\boldsymbol{g} = [g_1, \ldots, g_m]^T$ and discretizing the target space into voxels $\boldsymbol{r} = [r_1, \ldots, r_n]^T$, the integral in Eq.(1) can be replaced by matrix multiplication as

$$\boldsymbol{g} = \sum_{i=x,y,z} \sum_{j=x,y,z} \boldsymbol{H}_{ij}\boldsymbol{\chi}_{ij} = \boldsymbol{H}\boldsymbol{\chi} \tag{3}$$

where $\boldsymbol{H}_{ij}$ is the $m \times n$ sub-block of sensing matrix formed by the product of i component of the transmitting

field component and j component of the receiving field, i.e. $\boldsymbol{H}_{ij} = [E_{i,t}(\nu, r) \circ E_{j,r}(\nu, r)]$, for $i, j = x, y, z$. Rows and columns of $\boldsymbol{H}_{ij}$ correspond to frequency points (measurements) and discrete voxels receptively. $\boldsymbol{H}$ is the $m \times (n \times 9)$ complete sensing matrix formed by concatenating the sub-block sensing matrices as $[\boldsymbol{H}_{xx}, \boldsymbol{H}_{xy}, \ldots, \boldsymbol{H}_{zz}]$. And $\boldsymbol{\chi}_{ij}$ is the $n \times 1$ vectorized χ_{ij} of all voxels in the scene and $\boldsymbol{\chi}$ is the combined $(9 \times N) \times 1$ vector of χ_{ij} with $[\boldsymbol{\chi}_{xx}^T, \boldsymbol{\chi}_{xy}^T, \ldots, \boldsymbol{\chi}_{zz}^T]^T$. From Eq.(3), the nine sub-block sensing matrices $\boldsymbol{H}_{ij}$ interrogate the corresponding polarimetric scattering terms $\boldsymbol{\chi}_{ij}$ and coherently sum to the complex measurement. The polarimetric responses are reconstructed by solving a least-squares problem posed as

$$\hat{\boldsymbol{\chi}}(\boldsymbol{r}) = \arg\min_{\boldsymbol{\chi}} \|\boldsymbol{g} - \boldsymbol{H}\boldsymbol{\chi}\|_2 \tag{4}$$

As examined in [22], the radiation fields from this metasurface antenna has low spatial correlation and pseudo-orthogonality over the nine sub-block sensing matrices. The correlation matrix is defined as

$$\boldsymbol{X}(m, n, p, q) = \boldsymbol{H}_{mn}^{\dagger}\boldsymbol{H}_{pq} = [\langle E_{m,t}^* E_{n,r}^* E_{p,t} E_{q,r} \rangle_v], \quad \text{for} \quad m, n, p, q = x, y, z \tag{5}$$

where $\langle \cdot \rangle_f$ denotes the ensemble average over the frequency points,i.e. different coherent measurements. For $(m, n) = (p, q)$ cases, the diagonal $\boldsymbol{X}$ represents the spatial diversity of fields of different frequency at different voxels. For $(m, n) \neq (p, q)$ cases, the randomness and low magnitude of $\boldsymbol{X}$ represents the polarization diversity of different frequency which ascertain low cross-talk among different polarimetric channels.

In our previous work [22], [40], the vector field is described in one Cartesian reference frame with E_x, E_y, E_z components. Since the wave in the near field is locally propagating in different directions, using Cartesian coordinates can not intuitively indicate the local polarization state. To better examine polarization states of the sensing fields in the radiative near field, we utilize 3D Jones vector and 3D polarization ellipse [47]. Jones vectors describe fully polarized state of paraxial fields where the local electric field vectors lie in a common transverse plane perpendicular to the propagation direction [5]. A Jones vector which can describe any fully polarized state consists of two in-plane complex amplitudes $[E_x e^{j\delta_x}, E_y e^{j\delta_y}]^T$ along two orthogonal axes. It corresponds to a polarization ellipse on the transverse plane given by points of $(Re\{E_x e^{j\delta_x} e^{-j\omega t}\}, Re\{E_y e^{j\delta_y} e^{-j\omega t}\})$ with t as the time. This ellipse illustrates the trajectory of the end-point on the electric vector rotating with time. While Jones vectors, or Stokes parameters, are originally limited to polarization states of 2D fields, many literature have derived the generalization for 3D non-paraxial case with the purpose of characterizing near field [47]–[51]. Without common propagation direction, the polarization state of random near field can be properly described by a 3×3 polarization coherence matrix. This matrix is generated by the second-order cross-spectral density of random fields at any point $\boldsymbol{r}$ [48]. The nine elements in the coherency matrix $\boldsymbol{W}_{3\times3}$ are

$$W_{ij}(\boldsymbol{r}, \omega) = \langle E_i^*(\boldsymbol{r}, \omega) E_j(\boldsymbol{r}, \omega) \rangle \tag{6}$$

where i and j denotes the index for Cartesian coordinates and $\langle \cdot \rangle$ is the ensemble average over all the realizations of the random fields. This 3×3 matrix is positive semi-definite Hermitian matrix which has three non-negative eigenvalues $\lambda_1, \lambda_2, \lambda_3$ and three corresponding orthogonal eigenvectors $\boldsymbol{u}_1, \boldsymbol{u}_2, \boldsymbol{u}_3$. The unit-norm complex eigenvector $\boldsymbol{u}_t$ can be in general form expressed as $[a_1 e^{j\delta_1}, a_2 e^{j\delta_2}, a_3 e^{j\delta_3}]^T$. This represents, in reality, a unit 3D Jones vector. The general 3D Jones vector is expressed as

$$\boldsymbol{E} = [E_x e^{j\delta_x}, E_y e^{j\delta_y}, E_z e^{j\delta_z}]^T \tag{7}$$

which has five real parameters excluding a common phase. It has been shown that this complex vector given by (7) with $e^{-j\omega t}$ term corresponds to an ellipse lying on an arbitrary plane in 3D space [48], as depicted in Fig.2(a). The local propagation direction is perpendicular to the plane that the polarization ellipse resides in. With the physical meaning of the eigenvectors, the coherence matrix can be decomposed into incoherent sum of three polarization states given by $\boldsymbol{u}_t$:

$$\boldsymbol{W}_{3\times3} = \sum_{t=1}^{3} \lambda_t \boldsymbol{u}_t \otimes \boldsymbol{u}_t^{\dagger} \tag{8}$$

where $\otimes$ is the outer product and $\dagger$ is conjugate transpose. The necessary and sufficient condition for the field to be fully polarized is that $\lambda_2 = \lambda_3 = 0$, equivalently rank$(\boldsymbol{W}) = 1$. Therefore, 3D Jones vectors alone are able to represent the 3D fully polarized state.

For the following study, the sensing field radiated by the cavity-backed aperture antenna is considered as fully polarized everywhere within the imaging domain. Therefore, the 3D polarization state is represented by 3D Jones vector and the polarization ellipse included above. Figure 2(b)(c) illustrate the polarization ellipses of the transmitting(Tx) and receiving(Rx) sensing fields over a 0.2m $\times$ 0.2m 2D plane at $x = 0.3$m from the front surface of the antenna. The polarization ellipses for four neighboring frequency points are illustrated against the gray-scale as the magnitude of the sensing fields. It demonstrates the diverse polarization states (different orientation of the major axes and different local propagation directions) over the target scene. Each voxel in the scene experiences a series of different combinations of polarization states on the Tx and Rx ends, as depicted in Fig.2(a). The red and blue ellipses are the Tx and Rx sensing field polarization at five subsequent frequency points. This imaging system is retrieving the full 3D polarimetric response by measuring and receiving with a large number (frequency points) of different in-plane polarization states and different local propagation directions. It should be noted that these ellipses correspond to electric fields of different temporal frequencies. We assume that the polarimetric response $\boldsymbol{\chi}$ of the target has low temporal dispersion in the

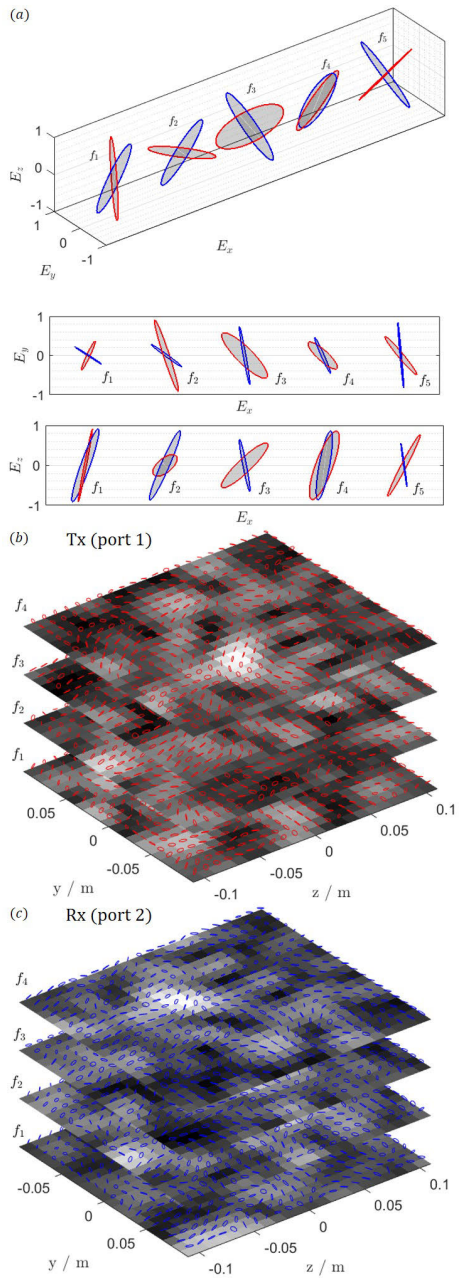

FIGURE 2. (a) Polarization ellipses at five subsequent frequency points. Red is the transmitting field and blue is receiving field. Polarization ellipses in $y-x$ and $z-x$ views are depicted. (b)(c) The gray-scale 2D figures are the sensing field magnitude at 4 subsequent frequency points. The 3D ellipsoids denote the polarization states at different locations in the scene.

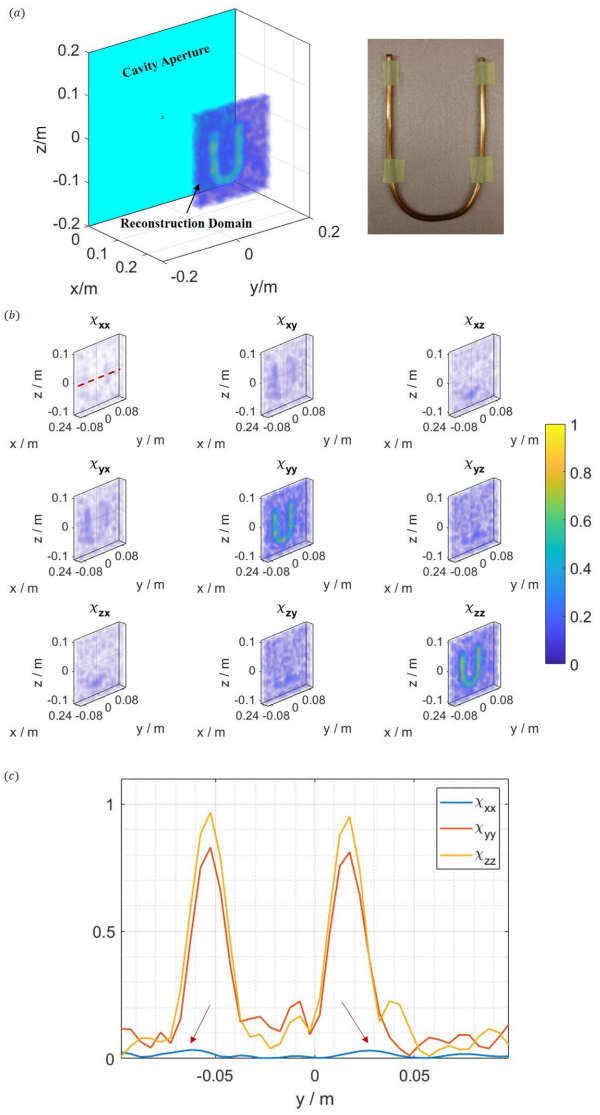

FIGURE 3. Reconstructed χ tensor for the Letter "U". (a) Imaging setup. The photo of letter'U' is shown. (b) Nine polarimetric channels of the χ matrix. The magnitude are normalized to global maximum among all nine channels. The opacity of each voxel is coded with the magnitude level. (c) The magnitude value of the three diagonal channels along the red dashed line depicted in χ_{xx}. Red arrows denote the reconstructed but small χ_{xx} value.

K-band we use and is more related to the polarization state described by the actual geometric feature of the polarization ellipses. Moreover, the reconstructed polarimetric response can be viewed as the averaged response over the bandwidth in the frequency sweep for a more general target.

III. CHARACTERISTIC XPOL-NULL POLARIZATION STATES IN 3D POLARIMETRY

In this section, we demonstrate the extraction of target characteristics from the experimentally reconstructed 3D polarimetric matrix $\boldsymbol{\chi}$ of a letter "U" target. This $13 \times 8\text{cm}^2$ target is made of a copper wire with a diameter of 5 mm, shown in Fig.3(a). This conductive wire is placed at $\hat{x} = 0.24$ cm, with the origin plane set at the near field scan location. The near fields of the aperture are characterized at around 10cm from the antenna aperture. Since the reconstruction uses the near fields directly, it is convenient to take the near field scan plane as the origin plane. From the definition of the field boundaries presented in [43], [52], we calculate the boundary distance between the reactive and radiative near-field region as $d_1 = 0.29$m and the distance between the radiative near-field and far-field regions as $d_2 = 3$m. The selected imaging distance is 0.24m from the near field scans, making it at $d = 0.34$m offset from the antenna aperture. It remains within this radiative near field range, $d_1 < d < d_2$.

A vector network analyzer (VNA, Agilent N5245A) takes S_{12} measurements $\boldsymbol{g}(f)$ at 4001 different frequency points evenly spaced within the K band from 17.5 GHz to 26.5 GHz.

The domain of interest is a $0.04\text{m}(\hat{x}) \times 0.2\text{m}(\hat{y}) \times 0.22\text{m}(\hat{z})$ cuboid and is discretized to $4 \times 40 \times 44$ voxels in three dimensions. Each voxel is of $10\text{mm}(\hat{x}) \times 5\text{mm}(\hat{y}) \times 5\text{mm}(\hat{z})$, determined by the range and cross-range resolution of this aperture antenna. Each voxel has a 3×3 complex matrix $\boldsymbol{\chi}$ to describe the averaged 3D polarimetric scattering response. The whole scene is reconstructed by solving Equation (4) with generalized minimal residue method (GMRES) [53], [54]. The symmetry of $\boldsymbol{\chi}$ is asserted by averaging the off-diagonal symmetric components, e.g., 'xy' and'yx'. The reconstructed polarimetric scattering matrix $\boldsymbol{\chi}$ of the letter "U" is illustrated in Fig.3(b) as nine different polarimetric channels.

The magnitude figures of nine channels are shown respectively in Fig.3(b). It demonstrates that our system is able to resolve target signatures in all nine polarimetric channels, as proved in [22]. Note that the resolution is not degraded for the polarimetric reconstruction compared to scalar reconstruction using the same measurements. However, the polarimetric information in the sub-resolution volume is the main usage of polarimetric imaging instead of the spatial resolution. The polarimetric responses are relatively small in the range ($\hat{x}$) related channels,e.g χ_{xx}, χ_{xz}, compared to the other four cross-range components (χ_{yy}, χ_{yz}, χ_{zy}, χ_{zz}). In the magnitude comparison of co-polarized components, illustrated in Fig.3(c), the co-polarized range channel $\boldsymbol{\chi}_{xx}$ tends to pick out the edge of the wire. It should be noted that despite small values, the two vertical parts of the letter 'U' have significant values of $\boldsymbol{\chi}_{yx}$, $\boldsymbol{\chi}_{xy}$ and the bottom part of the letter 'U' has a significant value of $\boldsymbol{\chi}_{xz}$, $\boldsymbol{\chi}_{zx}$. The range-related channels are inaccessible to the conventional 2D polarimetric imaging.

With the reconstructed 3D polarimetric matrix, in this paper, we aim to extract target parameters with physical meaning by extending the target decomposition methods of 2D polarimetry to 3D cases. The direct method for coherent polarimetric matrix is eigendecomposition-based analysis. We first formalize the 3D coherent power polarimetric matrix $\boldsymbol{G}_{3\times3}$ in an analogy to 2D Graves matrix $\boldsymbol{G}$, as shown at the bottom of the page, [5], where $*$ denotes complex conjugate. This matrix is positive-semidefinite which has three real non-negative eigenvalues $\lambda_1 \geqslant \lambda_2 \geqslant \lambda_3 \geqslant 0$ in non-increasing order and three corresponding orthonormal complex 3×1 eigenvectors $\boldsymbol{u}_1, \boldsymbol{u}_2, \boldsymbol{u}_3$, i.e.

$$\boldsymbol{G}[\boldsymbol{u}_1, \boldsymbol{u}_2, \boldsymbol{u}_3] = [\boldsymbol{u}_1, \boldsymbol{u}_2, \boldsymbol{u}_3] \begin{bmatrix} \lambda_1 & 0 & 0 \\ 0 & \lambda_2 & 0 \\ 0 & 0 & \lambda_3 \end{bmatrix}. \quad (9)$$

Each eigenvector $\boldsymbol{u}_i$ represents a unit 3D Jones vector which corresponds to some 3D polarization state. $(\boldsymbol{u}_1, \boldsymbol{u}_2, \boldsymbol{u}_3)$ form one complete set of 3D polarization bases under which the coherent power matrix $\boldsymbol{G}$ is diagonal. The 3D polarimetric matrix $\boldsymbol{\chi}$ can be diagonalized by a unitary transform of $\boldsymbol{U} = [\boldsymbol{u}_1, \boldsymbol{u}_2, \boldsymbol{u}_3]$ as

$$\boldsymbol{\chi}_D = \boldsymbol{U}^* \boldsymbol{\chi} \boldsymbol{U}^\dagger = \begin{bmatrix} \chi_1 & 0 & 0 \\ 0 & \chi_2 & 0 \\ 0 & 0 & \chi_3 \end{bmatrix}. \quad (10)$$

The transform format is different from ordinary unitary transform in the conjugate operation $*$ on $\boldsymbol{U}$ due to the choice of backscattering alignment coordinates. This diagonalization of $\boldsymbol{\chi}$ indicates that measuring cross-polarized scattering parameters of any combination within 3D polarization states given by $\boldsymbol{u}_1, \boldsymbol{u}_2, \boldsymbol{u}_3$ leads to zero. Therefore, eigenvectors $(\boldsymbol{u}_1, \boldsymbol{u}_2, \boldsymbol{u}_3)$ represent the local characteristic cross-polarization minimization (XPOL-Null) polarization states in the 3D polarimetry case. Compared to the XPOL-Null states in 2D polarimetry [5], the characteristic propagation direction is also recovered by these 3D Jones vector in addition to the in-plane polarization states. The three eigenvalues of $\boldsymbol{G}$ are proportional to the radar cross-section for the co-polarized scattering of corresponding XPOL-Null polarization states, similar to 2D polarimetry [5].

Following this process, three characteristic XPOL-Null polarization states are retrieved for every voxel of the letter "U" target using the reconstructed $\boldsymbol{\chi}$ matrices presented in Fig.3(b). Figure 4 illustrates three characteristic XPOL-Null polarization states $\boldsymbol{u}_i, i = 1, 2, 3$ by the corresponding 3D polarization ellipses. These ellipses all situate in different planes of 3D space. The plane of the first two XPOL-Null polarization ellipses $(\boldsymbol{u}_1, \boldsymbol{u}_2)$ is almost parallel to the transverse plane of this planar target. These two characteristic polarization states are similar to the two XPOL-Null states in 2D far-field polarimetry. Nevertheless, it is worth noting that these ellipses have projected areas along the range direction, which can be seen in the top-down view such that they do not fully reside in the transverse plane. The plane of the third XPOL-Null polarization ellipses $(\boldsymbol{u}_3)$ is predominantly perpendicular to the target plane. This range-related state is defined uniquely for the near-field polarimetry, different from the 2D case. For the in-plane orientation, the major axes of $\boldsymbol{u}_1$ ellipses (with the largest eigenvalues) align with the orientation of the copper wire. This is well demonstrated by the $\boldsymbol{u}_1$ ellipses on the two vertical bars of 'U' and the horizontal bottom of 'U'. The $\boldsymbol{u}_2$ states are orthogonal (not necessarily geometrically but in

$$\begin{aligned} \boldsymbol{G} &= \boldsymbol{\chi}^* \boldsymbol{\chi} \\ &= \begin{bmatrix} |\chi_{xx}|^2 + |\chi_{xy}|^2 + |\chi_{xz}|^2 & \chi_{xx}\chi_{xy}^* + \chi_{xy}\chi_{yy}^* + \chi_{xz}\chi_{zy}^* & \chi_{xx}\chi_{xz}^* + \chi_{xy}\chi_{yz}^* + \chi_{xz}\chi_{zz}^* \\ \chi_{yx}\chi_{xx}^* + \chi_{yy}\chi_{yx}^* + \chi_{yz}\chi_{zx}^* & |\chi_{xy}|^2 + |\chi_{yy}|^2 + |\chi_{zy}|^2 & \chi_{yx}\chi_{xz}^* + \chi_{yy}\chi_{yz}^* + \chi_{yz}\chi_{zz}^* \\ \chi_{zx}\chi_{xx}^* + \chi_{zy}\chi_{yx}^* + \chi_{zz}\chi_{zx}^* & \chi_{zx}\chi_{xy}^* + \chi_{zy}\chi_{yy}^* + \chi_{zz}\chi_{zy}^* & |\chi_{zx}|^2 + |\chi_{zy}|^2 + |\chi_{zz}|^2 \end{bmatrix} \end{aligned}$$

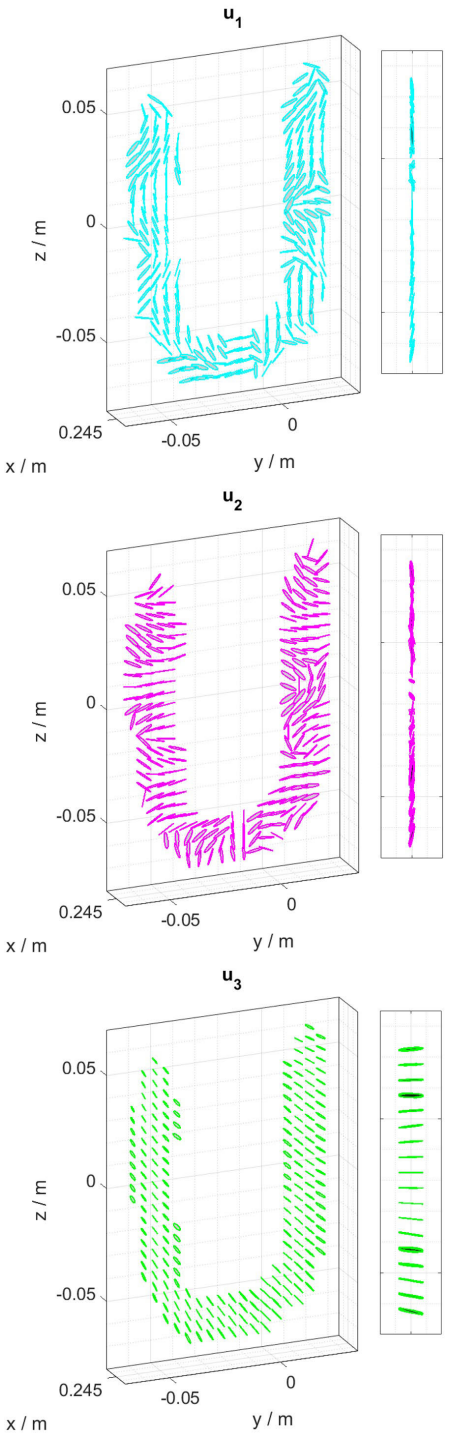

FIGURE 4. Eigenvectors of 3D coherent scattering power matrix of letter "U" target. The polarization ellipses represent u_1, u_2, u_3 respectively. Top-down view (*xy* plane) is given on the side.

the sense of polarization state) to first states $\boldsymbol{u}_1$ with primarily transverse components. As depicted in Fig.4, the major axes of $\boldsymbol{u}_2$ ellipses are, in reality, geometrically orthogonal to the orientation of the thin wire. This geometric orientation feature of $\boldsymbol{u}_1, \boldsymbol{u}_2$ polarization ellipses result from the local flat-surface like structure of copper wire, which has two orthogonal XPOL-Null polarization states parallel to the plane as in 2D polarimetry [5]. Moreover, in the macro view, fields polarized along the wire have a larger scattering response. Consequently, between $\boldsymbol{u}_1$ and $\boldsymbol{u}_2$,the XPOL-Null polarization states whose ellipses is along the wire have larger eigenvalues. These ellipses noticeably have small elliptical angles, and their shape is close to a line, which refers to a linear polarization state of different orientation in 3D space. This is valid for the metallic wire target since scattering from it should be anisotropic.

Eigenvalues of all the voxels that contain the target are compared in Fig.5. The eigenvalues are normalized by the trace of the 3D coherent power polarimetric matrix $\boldsymbol{G}$, i.e. $\hat{\lambda}_i = \lambda_i / tr(\boldsymbol{G})$, leaving the unit sum of all three eigenvalues for every voxel. The two larger eigenvalues are comparable, while the third eigenvalue for the primarily range XPOL-Null state is 10^{-4} smaller than the other two dominant ones. This is as expected since the eigenvalues of coherent power matrix $\boldsymbol{G}$ denotes the cross-section levels for different co-polarized XPOL-Null states. This planar thin wire target has a small scattering response in the range direction compared to the transverse dimensions.

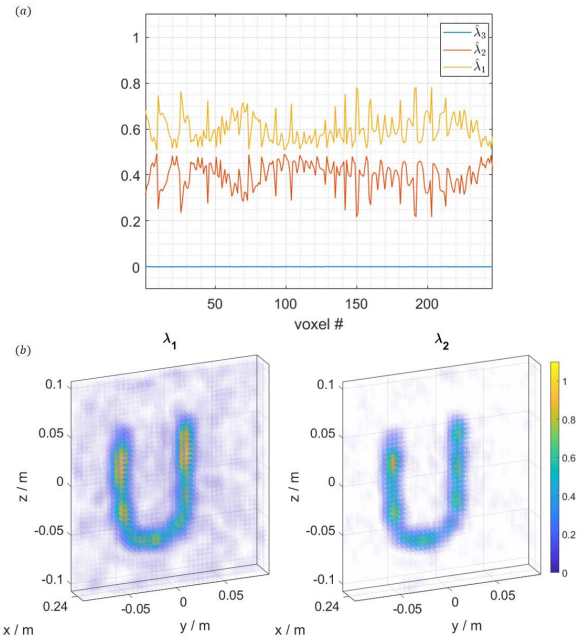

FIGURE 5. Eigenvalues of 3D coherent scattering power matrix of letter "U" target. (a) Three normalized eigenvalues for target voxels. (b) First two dominant eigenvalues in the reconstruction domain.

Figure 6 depicts the normal vector and the major-axis vector of $\boldsymbol{u}_1$ ellipses on one constant-height slice ($z = 0$m) crossing the two vertical bars of 'U'. The color of the vectors is given by the absolute value of three directional cosines [cos(a), cos(b), cos(c)] such that the vector is red when close to the $\hat{x}$ axis, green when close to the $\hat{y}$ axis and blue when close to the $\hat{z}$ axis. The top-down view of these vectors on a constant-z slice in Fig.6 clearly illustrates that the normal vector (red) rotates along the curved surface of the wire while

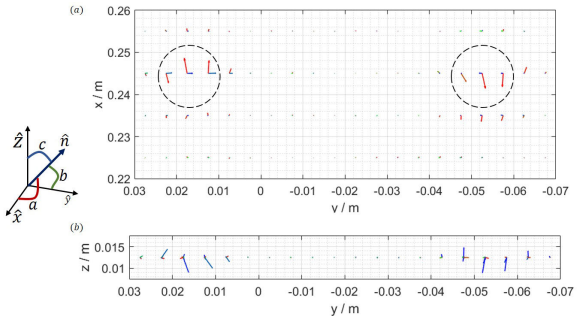

FIGURE 6. (a) Top-down view of the direction vectors on the constant-z plane ($z = 0$m) Black dashed circles denotes the location of the letter 'U'. (b) Front view of the aforementioned constant-z plane.

the major-axis vector not fully points along the wire direction but with some angle to the wire and distributed symmetrically with regard to the center-line of the wire. These detailed local structure information offers more insights into the detailed features of the target, which is not deliverable by conventional 2D polarimetry. The presented result is a testament to the advantage of near-field operation in that range probing of the target is achieved, extending the conventional 2×2 polarization bases in far-field to 3×3 by also leveraging the range component.

IV. TARGET PARAMETERIZATION OF 3D POLARIMETRY

In this section, we propose to parameterize the XPOL-Null states and the diagonalized $\boldsymbol{\chi}$ matrix to further quantitatively characterize the target with 3D polarimetry data. Take the first eigenvector $\boldsymbol{u}_1$. As shown above, each eigenvector refers to an ellipse oriented arbitrarily in 3D space, as shown in Fig.7(a). There exists a real rotation matrix $\boldsymbol{o}_{3\times3}$ such that $\boldsymbol{o}^T\boldsymbol{u}_1$ is the same ellipse rotated to coincide with the Y_0Z_0 plane and the major axis of the rotated ellipse coincide with Y_0 axis. Let $\boldsymbol{u}_1 = [a_x e^{\mathrm{j}\phi_1}, a_y e^{\mathrm{j}\phi_2}, a_z e^{\mathrm{j}\phi_3}]^T$, and the rotation process is expressed as

$$\boldsymbol{o}^T\boldsymbol{u}_1 = [0, a_y, a_z e^{\pm \mathrm{j}\pi/2}]^T, \tag{11}$$

where $\boldsymbol{o}$ is a 3×3 orthonormal real matrix denotes a 3D rotation. This rotation matrix can be determined by finding the unit vectors of the intrinsic axes $\hat{x}_1, \hat{y}_1, \hat{z}_1$ affixed to the ellipse, maintaining the right-handedness. Then the rotation matrix is found to be $\boldsymbol{o} = [\hat{x}_1, \hat{y}_1, \hat{z}_1]$. The rotation matrix can be represented by three Euler angles α, β, γ [55]. Following the extrinsic rotation sequence of ZYX, the three Euler angles can be found by comparing the rotation matrix $\boldsymbol{o}$ with [56]

$$Z_1Y_2X_3 = \begin{bmatrix} c_1c_2 & c_1s_2s_3 - c_3s_1 & s_1s_3 + c_1c_3s_2 \\ c_2s_1 & c_1c_3 + s_1s_2s_3 & c_3s_1s_2 - c_1s_3 \\ -s_2 & c_2s_3 & c_2c_3 \end{bmatrix} \tag{12}$$

where 1, 2, 3 are the three Euler angles α, β, γ and c, s denote cosine and sine respectively. Since the rotation matrix $\boldsymbol{o}$ is defined by the rotation from the in-plane ellipse $\boldsymbol{o}^T\boldsymbol{u}_1$ to the 3D ellipse $\boldsymbol{u}_1$, the rotation process can be viewed as a sequence of three elementary extrinsic rotations as such: 1) a rotation of γ around X_0 axis; 2) a rotation of β around Y_0 axis; 3) a rotation of α around Z_0 axis. The three Euler rotation angles of the first eigenvector $\boldsymbol{u}_1$ of the letter 'U' are depicted in Fig.7(b-d). The Euler angles of the other two eigenvectors $\boldsymbol{u}_2, \boldsymbol{u}_3$ can be found with the same process.

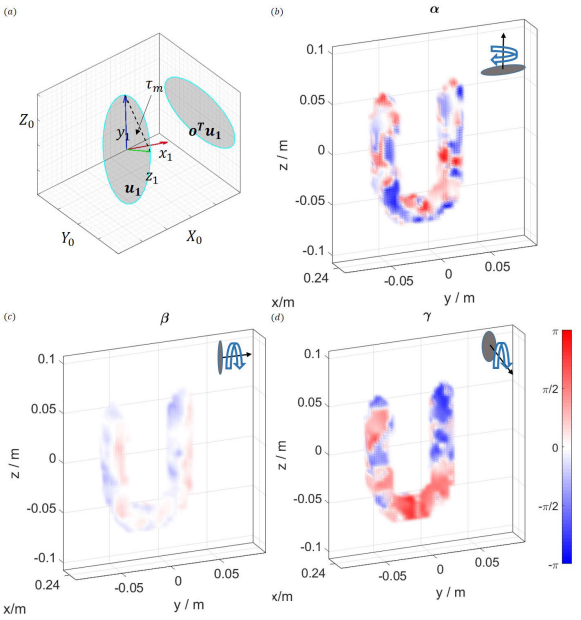

FIGURE 7. (a)Polarization ellipse in 3D space and the rotated ellipse to lie in the YZ plane. (b)(c)(d)Three Euler angles (ZYX sequence) of the first eigenvector $\boldsymbol{u}_1$.

Similar to the helicity angle in 2D polarimetry, the ellipticity angle τ_m of the 3D polarization ellipses also denotes the anisotropy of the scattering with 0 as the anisotropic scattering and $\pi/4$ as the isotropic scattering. For the 3D case, the ellipticity angle can be easily found in the rotated in-plane ellipse $\boldsymbol{o}^T\boldsymbol{u}_1$ by simply retrieving the inverse tangent of a_z/a_y. The in-plane ellipticity angle of the first XPOL-Null polarization state of the letter 'U' is shown in Fig.8. The angle τ_m is close to zero for points on the target, indicating the anisotropic scattering of this metallic target.

Using the rotation matrix and the Euler angles, the geometric rotation parameters of α, β, γ and the anisotropy parameter τ_m can be found for the three XPOL-Null polarization states. Under the polarization bases formed by XPOL-Null polarization states, the 3D polarimetric matrix $\boldsymbol{\chi}$ is diagonal, and it can be parameterized in the similar way as Huynen did for the 2D polarimetric coherent polarimetric matrix [7]. The diagonalized polarimetric matrix $\boldsymbol{\chi}_D$ can be written in the general form of

$$\begin{aligned} \boldsymbol{\chi}_D &= \begin{bmatrix} \chi_1 & 0 & 0 \\ 0 & \chi_2 & 0 \\ 0 & 0 & \chi_3 \end{bmatrix} \\ &= me^{\mathrm{j}\delta} \begin{bmatrix} 1 & 0 & 0 \\ 0 & \tan^2\gamma_1 e^{-\mathrm{j}4\nu_1} & 0 \\ 0 & 0 & \tan^2\gamma_2 e^{-\mathrm{j}4\nu_2} \end{bmatrix} \end{aligned}$$

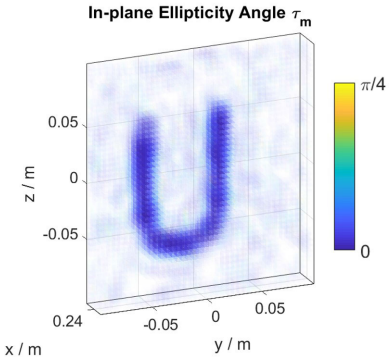

FIGURE 8. In-plane helicity angle (ellipticity angle of the ellipse).

in an analogy to 2D Euler parameter definition [5]. γ denotes the common phase term. γ_1 and γ_2 denote the magnitude ratio between the co-polarized scattering parameters of the three XPOL-Null polarization states. It is related to the target polarization sensibility to different states. It ranges from $\pi/4$ for a flat surface target which has no preference over the two orthogonal XPOL-Null polarization states, to 0 for a linear dipole-like target which has stronger response in one XPOL-Null polarization state than the other. ν is the phase difference between the co-polarized scattering responses between two XPOL-Null states, which is related to scattering bounce times. It also changes from phase difference of $(\pi/4)$, meaning double or multiple bounces to 0 difference means single bounce. Figure 9 illustrates the distribution of these four target parameters on the target. $\gamma_{1,2}$ is close to $\pi/4$ at most points on the target, suggesting that every local point has no dominant preference over the first two XPOL-Null states after leaving out the local surface orientation effect. It is the situation that every point on the wire target would locally have identical polarimetric scattering sensitivity. $\gamma_{1,3}$ is close

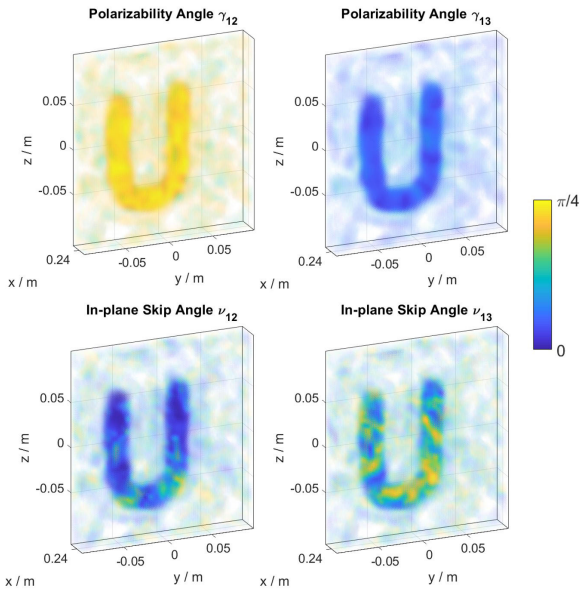

FIGURE 9. Four generalized target parameters (γ_{12}, γ_{13}, ν_{12}, ν_{13}) for the letter "U" target.

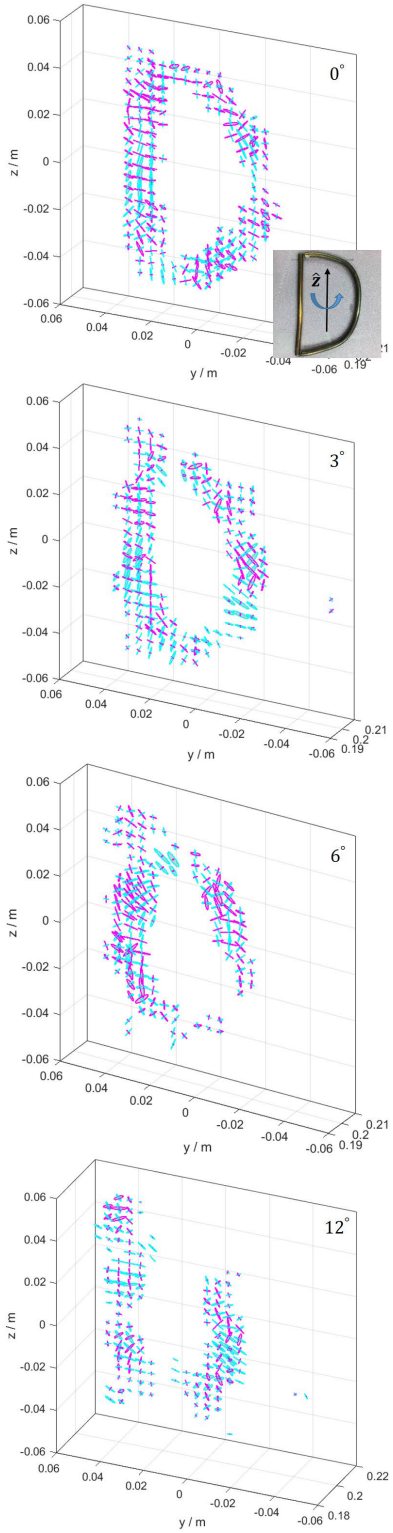

FIGURE 10. Two orthogonal XPOL-Null polarization ellipses (cyan and magenta) of letter "D" with rotation angle of 0°, 3°, 6° and 12° with respect to $\hat{z}$ axis.

to zero due to the extremely small response in the range direction. The in-plane skip angle ν_{12} is zero for most points while the two corners of the letter 'U' have the double bounce scattering. More points have large ν_{13} values due to stronger

multiple scattering when the wave is traveling parallel to the target plane.

V. IMAGING TARGET WITH ROTATION IN SPACE

In this section, we apply the computational polarimetric imaging scheme to a letter ''D'' wire target with different rotation in three dimensions and a planar target made of copper tapes. These results serve to demonstrate the consistency of the proposed target parameterization in describing the 3D polarimetric scattering characteristics. The letter ''D'' target, depicted in Fig.10 inset, is made of copper wire bent to form the D shape, placed at around 0.20 m in front of the metasurface aperture. We studied how XPOL-Null polarization states would change with the rotation of the target. When the target is rotated, different sections of the spherical cylinder part of the letter ''D'' are seen by the metasurface aperture. Figure 10 illustrates the two orthogonal XPOL-Null polarization states of the letter ''D'' with four different rotation angles (0°, 3°, 6° and 12°) with respect to $\hat{z}$ axis. For the rotation angles where the reflected signal is not captured by the metasurface aperture, the corresponding parts of the object can not be visible in the reconstructions. However, this is not a limitation of the polarimetric imaging technique but rather a physical phenomenon of reflection specularity that applies to monostatic imaging systems in general. From the reconstructed part of the target, the XPOL-Null polarization ellipses rotate along with the change in the position of the letter ''D'' to the antenna aperture. The polarization ellipses consistently demonstrate the local geometric structure by examining the orientation of the ellipse plane and the major-axis direction.

VI. CONCLUSION

A scheme of computational polarimetric imaging using a cavity-backed metasurface aperture antenna has been presented. The sensing fields from the cavity-backed metasurface aperture antenna has low spatial correlation and diversity of polarization states to multiplex the 3D polarimetric response over the image domain into a single complex measurement. Built on our preliminary work, we have further characterized the spatially varying but locally fully polarized coherent random fields from the metasurface antenna using generalized Jones vector and polarization ellipses in 3D space. From the diagonalization process of the 3D polarimetric matrix, three orthogonal XPOL-Null polarization states have been retrieved. It has been shown that the orientation of the major axis and the ellipse plane offers insight into the local geometric structure and scattering mechanism. Euler angles denoting the rotation matrix can be retrieved from the ellipse plane. After leaving out the effects of rotation, the in-plane ellipticity angle of the polarization ellipse yields information of the scattering anisotropy. Four generalized coherent target parameters are retrieved from the diagonalized polarimetric matrix, which serve for the polarization sensitivity and multi-scattering. Imaging results of different targets consolidate our 3D polarimetry scheme modeling for consistently characterizing the 3D polarimetric scattering response of the target. Furthermore, the assumptions made here for establishing the 3D matrix model are still valid for different frequencies, and therefore, this technique could readily be implemented at higher frequencies, including millimeter-wave and terahertz frequencies for more application scenarios.

REFERENCES

[1] W. L. Cameron, N. N. Youssef, and L. K. Leung, ''Simulated polarimetric signatures of primitive geometrical shapes,'' *IEEE Trans. Geosci. Remote Sens.*, vol. 34, no. 3, pp. 793–803, May 1996.
[2] I. Hajnsek, E. Pottier, and S. R. Cloude, ''Inversion of surface parameters from polarimetric SAR,'' *IEEE Trans. Geosci. Remote Sens.*, vol. 41, no. 4, pp. 727–744, Apr. 2003.
[3] H. A. Zebker and J. J. Van Zyl, ''Imaging radar polarimetry: A review,'' *Proc. IEEE*, vol. 79, no. 11, pp. 1583–1606, 1991.
[4] D. L. Evans, T. G. Farr, J. J. van Zyl, and H. A. Zebker, ''Radar polarimetry: Analysis tools and applications,'' *IEEE Trans. Geosci. Remote Sens.*, vol. 26, no. 6, pp. 774–789, Nov. 1988.
[5] J.-S. Lee and E. Pottier, *Polarimetric Radar Imaging: From Basics to Applications*. Boca Raton, FL, USA: CRC Press, 2009.
[6] A. Guissard, ''Mueller and kennaugh matrices in radar polarimetry,'' *IEEE Trans. Geosci. Remote Sens.*, vol. 32, no. 3, pp. 590–597, May 1994.
[7] J. R. Huynen, ''Phenomenological theory of radar targets,'' Ph.D. dissertation, Technical Univ., Delft, The Netherlands, 1970.
[8] S. R. Cloude and E. Pottier, ''A review of target decomposition theorems in radar polarimetry,'' *IEEE Trans. Geosci. Remote Sens.*, vol. 34, no. 2, pp. 498–518, Mar. 1996.
[9] A. Freeman and S. L. Durden, ''A three-component scattering model for polarimetric SAR data,'' *IEEE Trans. Geosci. Remote Sens.*, vol. 36, no. 3, pp. 963–973, May 1998.
[10] S. R. Cloude and E. Pottier, ''An entropy based classification scheme for land applications of polarimetric SAR,'' *IEEE Trans. Geosci. Remote Sens.*, vol. 35, no. 1, pp. 68–78, Jan. 1997.
[11] J.-S. Lee, M. R. Grunes, E. Pottier, and L. Ferro-Famil, ''Unsupervised terrain classification preserving polarimetric scattering characteristics,'' *IEEE Trans. Geosci. Remote Sens.*, vol. 42, no. 4, pp. 722–731, Apr. 2004.
[12] H. H. Lim, A. A. Swartz, H. A. Yueh, J. A. Kong, R. T. Shin, and J. J. Van Zyl, ''Classification of Earth terrain using polarimetric synthetic aperture radar images,'' *J. Geophys. Res., Solid Earth*, vol. 94, no. B6, pp. 7049–7057, 1989.
[13] R. D. West, T. E. LaBruyere, III, J. Skryzalin, K. M. Simonson, R. L. Hansen, and M. H. Van Benthem, ''Polarimetric SAR image terrain classification,'' *IEEE J. Sel. Topics Appl. Earth Observ. Remote Sens.*, vol. 12, no. 11, pp. 4467–4485, Nov. 2019.
[14] Y. Oh, K. Sarabandi, and F. T. Ulaby, ''An inversion algorithm for retrieving soil moisture and surface roughness from polarimetric radar observation,'' in *Proc. IEEE Int. Geosci. Remote Sens. Symp. (IGARSS)*, vol. 3, Aug. 1994, pp. 1582–1584.
[15] Y. Kim and J. J. van Zyl, ''A time-series approach to estimate soil moisture using polarimetric radar data,'' *IEEE Trans. Geosci. Remote Sens.*, vol. 47, no. 8, pp. 2519–2527, Aug. 2009.
[16] S. H. Yueh, W. J. Wilson, and S. Dinardo, ''Polarimetric radar remote sensing of ocean surface wind,'' *IEEE Trans. Geosci. Remote Sens.*, vol. 40, no. 4, pp. 793–800, Apr. 2002.
[17] B. Zhang, W. Perrie, P. W. Vachon, X. Li, W. G. Pichel, J. Guo, and Y. He, ''Ocean vector winds retrieval from C-band fully polarimetric SAR measurements,'' *IEEE Trans. Geosci. Remote Sens.*, vol. 50, no. 11, pp. 4252–4261, Nov. 2012.
[18] J. Ellis and A. Dogariu, ''Optical polarimetry of random fields,'' *Phys. Rev. Lett.*, vol. 95, no. 20, Nov. 2005, Art. no. 203905.
[19] J. J. Gil, A. T. Friberg, T. Setälä, and I. S. José, ''Structure of polarimetric purity of three-dimensional polarization states,'' *Phys. Rev. A, Gen. Phys.*, vol. 95, no. 5, May 2017, Art. no. 053856.
[20] M. Migliaccio, J. J. Gil, A. Sorrentino, F. Nunziata, and G. Ferrara, ''The polarization purity of the electromagnetic field in a reverberating chamber,'' *IEEE Trans. Electromagn. Compat.*, vol. 58, no. 3, pp. 694–700, Jun. 2016.
[21] M. Migliaccio, A. Sorrentino, F. Nunziata, J. J. Gil, and S. Cappa, ''Components of purity to describe the polarimetric state of a 3-D field within the reverberating chamber,'' *IEEE Trans. Electromagn. Compat.*, early access, May 27, 2020, doi: 10.1109/TEMC.2020.2993898.
[22] T. Fromenteze, O. Yurduseven, M. Boyarsky, J. Gollub, D. L. Marks, and D. R. Smith, ''Computational polarimetric microwave imaging,'' *Opt. Express*, vol. 25, no. 22, pp. 27488–27505, 2017.

[23] J. Romberg, "Imaging via compressive sampling," *IEEE Signal Process. Mag.*, vol. 25, no. 2, pp. 14–20, Mar. 2008.
[24] W. L. Chan, M. L. Moravec, R. G. Baraniuk, and D. M. Mittleman, "Terahertz imaging with compressed sensing and phase retrieval," *Opt. Lett.*, vol. 33, no. 9, pp. 974–976, 2008.
[25] S. S. Welsh, M. P. Edgar, R. Bowman, P. Jonathan, B. Sun, and M. J. Padgett, "Fast full-color computational imaging with single-pixel detectors," *Opt. Express*, vol. 21, no. 20, pp. 23068–23074, 2013.
[26] J. D. Shea, P. Kosmas, B. D. Van Veen, and S. C. Hagness, "Contrast-enhanced microwave imaging of breast tumors: A computational study using 3D realistic numerical phantoms," *Inverse Problems*, vol. 26, no. 7, Jul. 2010, Art. no. 074009.
[27] D. Shin, A. Kirmani, V. K. Goyal, and J. H. Shapiro, "Photon-efficient computational 3-D and reflectivity imaging with single-photon detectors," *IEEE Trans. Comput. Imag.*, vol. 1, no. 2, pp. 112–125, Jun. 2015.
[28] G. Zheng, R. Horstmeyer, and C. Yang, "Wide-field, high-resolution Fourier ptychographic microscopy," *Nature Photon.*, vol. 7, no. 9, p. 739, 2013.
[29] D. L. Marks, D. S. Kittle, H. S. Son, S. H. Youn, S. D. Feller, J. Kim, D. J. Brady, D. R. Golish, E. M. Vera, M. E. Gehm, R. A. Stack, E. J. Tremblay, and J. E. Ford, "Gigapixel imaging with the AWARE multiscale camera," *Opt. Photon. News*, vol. 23, no. 12, p. 31, 2012.
[30] B. Sun, M. P. Edgar, R. Bowman, L. E. Vittert, S. Welsh, A. Bowman, and M. J. Padgett, "3D computational imaging with single-pixel detectors," *Science*, vol. 340, no. 6134, pp. 844–847, May 2013.
[31] M. F. Duarte, M. A. Davenport, D. Takhar, J. N. Laska, T. Sun, K. F. Kelly, and R. G. Baraniuk, "Single-pixel imaging via compressive sampling," *IEEE Signal Process. Mag.*, vol. 25, no. 2, pp. 83–91, Mar. 2008.
[32] Z. Zhang, X. Ma, and J. Zhong, "Single-pixel imaging by means of Fourier spectrum acquisition," *Nature Commun.*, vol. 6, p. 6225, Feb. 2015.
[33] J. Hunt, J. Gollub, T. Driscoll, G. Lipworth, A. Mrozack, M. S. Reynolds, D. J. Brady, and D. R. Smith, "Metamaterial microwave holographic imaging system," *J. Opt. Soc. Amer. A, Opt. Image Sci.*, vol. 31, no. 10, pp. 2109–2119, Oct. 2014.
[34] T. Sleasman, M. F. Imani, J. N. Gollub, and D. R. Smith, "Dynamic metamaterial aperture for microwave imaging," *Appl. Phys. Lett.*, vol. 107, no. 20, Nov. 2015, Art. no. 204104.
[35] T. Fromenteze, O. Yurduseven, M. F. Imani, J. Gollub, C. Decroze, D. Carsenat, and D. R. Smith, "Computational imaging using a mode-mixing cavity at microwave frequencies," *Appl. Phys. Lett.*, vol. 106, no. 19, May 2015, Art. no. 194104.
[36] J. N. Gollub, O. Yurduseven, K. P. Trofatter, D. Arnitz, M. F. Imani, T. Sleasman, M. Boyarsky, A. Rose, A. Pedross-Engel, H. Odabasi, T. Zvolensky, G. Lipworth, D. Brady, D. L. Marks, M. S. Reynolds, and D. R. Smith, "Large metasurface aperture for millimeter wave computational imaging at the human-scale," *Sci. Rep.*, vol. 7, no. 1, p. 42650, May 2017.
[37] D. L. Marks, O. Yurduseven, and D. R. Smith, "Cavity-backed metasurface antennas and their application to frequency diversity imaging," *J. Opt. Soc. Amer. A, Opt. Image Sci.*, vol. 34, no. 4, pp. 472–480, 2017.
[38] O. Yurduseven, T. Fromenteze, D. L. Marks, J. N. Gollub, and D. R. Smith, "Frequency-diverse computational microwave phaseless imaging," *IEEE Antennas Wireless Propag. Lett.*, vol. 16, pp. 2808–2811, 2017.
[39] T. Fromenteze, X. Liu, M. Boyarsky, J. Gollub, and D. R. Smith, "Phaseless computational imaging with a radiating metasurface," *Opt. Express*, vol. 24, no. 15, pp. 16760–16776, 2016.
[40] O. Yurduseven, T. Fromenteze, R. Peng, and D. R. Smith, "Frequency-diverse computational polarimetic imaging," in *Proc. 13th Eur. Conf. Antennas Propag. (EuCAP)*, Mar. 2019, pp. 1–4.
[41] A. C. Tondo Yoya, B. Fuchs, and M. Davy, "Computational passive imaging of thermal sources with a leaky chaotic cavity," *Appl. Phys. Lett.*, vol. 111, no. 19, Nov. 2017, Art. no. 193501.
[42] J. Adametz and L.-P. Schmidt, "Threat object classification with a close range polarimetric imaging system by means of H-α decomposition," *Int. J. Microw. Wireless Technol.*, vol. 6, nos. 3–4, pp. 415–421, Jun. 2014.
[43] C. A. Balanis, *Advanced Engineering Electromagnetics*. Hoboken, NJ, USA: Wiley, 1999.
[44] W. Ren, "Dyadic Green's functions and dipole radiations in layered chiral media," *J. Appl. Phys.*, vol. 75, no. 1, pp. 30–35, Jan. 1994.
[45] G. Lipworth, A. Rose, O. Yurduseven, V. R. Gowda, M. F. Imani, H. Odabasi, P. Trofatter, J. Gollub, and D. R. Smith, "Comprehensive simulation platform for a metamaterial imaging system," *Appl. Opt.*, vol. 54, no. 31, pp. 9343–9353, 2015.
[46] K. Langenberg, M. Brandfass, P. Fellinger, T. Gurke, and T. Kreutter, "A unified theory of multidimensional electromagnetic vector inverse scattering within the kirchhoff or born approximation," in *Radar Target Imaging*. Berlin, Germany: Springer, 1994, pp. 113–151.
[47] T. Carozzi, R. Karlsson, and J. Bergman, "Parameters characterizing electromagnetic wave polarization," *Phys. Rev. E, Stat. Phys. Plasmas Fluids Relat. Interdiscip. Top.*, vol. 61, no. 2, p. 2024, 2000.
[48] J. Ellis, A. Dogariu, S. Ponomarenko, and E. Wolf, "Correlation matrix of a completely polarized, statistically stationary electromagnetic field," *Opt. Lett.*, vol. 29, no. 13, pp. 1536–1538, 2004.
[49] M. R. Dennis, "Geometric interpretation of the three-dimensional coherence matrix for nonparaxial polarization," *J. Opt. A, Pure Appl. Opt.*, vol. 6, no. 3, pp. S26–S31, Mar. 2004.
[50] C. J. R. Sheppard, "Jones and Stokes parameters for polarization in three dimensions," *Phys. Rev. A, Gen. Phys.*, vol. 90, no. 2, Aug. 2014, Art. no. 023809.
[51] T. Setälä, A. Shevchenko, M. Kaivola, and A. T. Friberg, "Degree of polarization for optical near fields," *Phys. Rev. E, Stat. Phys. Plasmas Fluids Relat. Interdiscip. Top.*, vol. 66, no. 1, Jul. 2002, Art. no. 016615.
[52] D. Slater, *Near-Field Antenna Measurements*. Norwood, MA, USA: Artech House, 1991.
[53] Y. Saad and M. H. Schultz, "GMRES: A generalized minimal residual algorithm for solving nonsymmetric linear systems," *SIAM J. Sci. Stat. Comput.*, vol. 7, no. 3, pp. 856–869, Jul. 1986.
[54] O. Yurduseven, M. F. Imani, H. Odabasi, J. Gollub, G. Lipworth, A. Rose, and D. R. Smith, "Resolution of the frequency diverse metamaterial aperture imager," *Prog. Electromagn. Res.*, vol. 150, pp. 97–107, 2015.
[55] J. B. Kuipers, *Quaternions and Rotation Sequences*, vol. 66. Princeton, NJ, USA: Princeton Univ. Press, 1999.
[56] G. G. Slabaugh, "Computing Euler angles from a rotation matrix," *Retrieved August*, vol. 6, no. 2000, pp. 39–63, 1999.

RIXI PENG received the bachelor's degree in optical engineering from Tsinghua University, Beijing. He is currently pursuing the Ph.D. degree in metamaterial with Duke University, Durham, NC. His research interest includes the design of polarimetric metamaterial device and the applications of novel metamaterial antenna in microwave polarimetric imaging.

OKAN YURDUSEVEN (Senior Member, IEEE) received the B.Sc. and M.Sc. degrees in electrical engineering from Yildiz Technical University, Istanbul, Turkey, in 2009 and 2011, respectively, and the Ph.D. degree in electrical engineering from Northumbria University, Newcastle upon Tyne, U.K., in 2014. He is currently a Senior Lecturer (Associate Professor) with the School of Electronics, Electrical Engineering and Computer Science, Queen's University Belfast, U.K. He is also an Adjunct Assistant Professor with Duke University, USA. From 2018 to 2019, he was a NASA Postdoctoral Fellow with the Jet Propulsion Laboratory, California Institute of Technology, USA. From 2014 to 2018, he was a Postdoctoral Research Associate with the Department of Electrical and Computer Engineering, Duke University. His research interests include microwave and millimeter-wave imaging, multiple-input-multiple-output (MIMO) radar, wireless power transfer, antennas and propagation, antenna measurement techniques, and metamaterials. He has authored more than 100 peer-reviewed technical journal and conference papers. He has served as a technical program committee member and a guest editor for several conferences and journals in these fields. In 2017, he received an Outstanding Postdoctoral Award from Duke University. He was a recipient of the NASA Postdoctoral Program Fellowship administrated by Universities Space Research Association (USRA) in 2018. In 2019, in collaboration with the University of Limoges, France, he received the Alliance Hubert Curien Award funded by the British Council. In 2020, he was bestowed the Leverhulme Trust Research Leadership Award. He is a member of the European Association on Antennas and Propagation (EurAAP).

THOMAS FROMENTEZE received the Ph.D. degree from the University of Limoges, Limoges, France, in 2015. From 2015 to 2016, he was a Postdoctoral Researcher with Duke University, Durham, NC, USA. He is currently a Maître de Conférences (Assistant Professor) with the Xlim Research Institute, University of Limoges. He is also an Adjunct Assistant Professor with the Center for Metamaterials and Integrated Plasmonics, Duke University. His research interests include ultra-wideband microwave and millimeter-wave imaging, wave propagation in complex media, computational/compressive imaging, and the various associated inverse problems. He received the 11th EuRAD Young Engineer Prize during the European Microwave Week 2015.

DAVID R. SMITH (Senior Member, IEEE) received the B.S. and Ph.D. degrees in physics from the University of California at San Diego, San Diego, CA, USA, in 1994 and 1998, respectively. He is the James B. Duke Distinguished Professor with the Electrical and Computer Engineering Department, Duke University, where he also serves as the Director for the Center for Metamaterial and Integrated Plasmonics. He holds a secondary faculty appointment in the Physics Department, Duke University. He is a Visiting Professor of physics with Imperial College, London, U.K. He has over 300 publications in the area of metamaterials and more than 100 patents and patent filings. He and his colleagues demonstrated the first left-handed (or negative index) metamaterial at microwave frequencies in 2000. In 2006, he and his colleague Sir John Pendry reported a new electromagnetic design approach, now termed transformation optics, and suggested the possibility of a metamaterial invisibility cloak. His group subsequently demonstrated a metamaterial invisibility cloak later, in 2006. His research interests include the theory, simulation, and characterization of unique structures across the electromagnetic spectrum, including photonic crystals, metamaterials, and plasmonic nanostructures. He was part of a five-member team that received the Descartes Research Prize in 2005, awarded by the European Union, for contributions to metamaterials and other novel electromagnetic materials. Since 2009, he has been named a Citation Laureate by Clarivate Analytics Web of Science, for having among the most number of highly cited articles in the field of physics. He was a co-recipient of the McGroddy Prize for New Materials, awarded by the American Physical Society, for the Discovery of Metamaterials in 2013. In 2016, he was elected to the National Academy of Inventors. He has recently been active in transitioning metamaterial concepts for commercialization, being a Co-Founder of Evolv Technology, Echodyne Corporation, Pivotal Communications, and an Advisor to Kymeta Corporation and Lumotive Corporation-all companies devoted to developing metamaterial products. More recently, he has led efforts to apply metasurface apertures for use in computational imaging, with an emphasis on security screening using millimeter waves.